Coulomb stress changes in Hesperia Planum, Mars, reveal regional thrust fault reactivation

Cheryl L. Goudy and Richard A. Schultz
Department of Geological Sciences and Engineering, University of Nevada, Reno, Nevada, USA

Tracy K. P. Gregg
Department of Geological Sciences, State University of New York at Buffalo, Buffalo, New York, USA

Received 10 May 2004; revised 28 February 2005; accepted 19 May 2005; published 29 October 2005.

[1] The orthogonal pattern of NE and NW striking wrinkle ridges in Hesperia Planum makes this area unique and enigmatic. The wrinkle ridge morphologies revealed in Mars Orbiter Laser Altimeter topography across ridge structures in Hesperia Planum suggest that wrinkle ridges form above thrust faults. The timing relationship among wrinkle ridge sets is evident in the digital elevation models; thrust faults striking NE are older than the NW striking ridges. The NE striking wrinkle ridges show unequal development adjacent to the NW striking wrinkle ridges, and an echelon pattern throughout Hesperia Planum; therefore formation by two independent sequential sets is not likely. Reactivation of the older (NE) thrust faults from the younger (NW) wrinkle ridges, inferred from the observations, is tested by resolving Coulomb failure stress changes along the older thrust faults from slip along the younger thrust faults. We find fault reactivation is likely in Hesperia Planum, regardless of the deposit material (basalt or tuff). Previously, the NE striking wrinkle ridges were interpreted as forming prior to, or contemporaneous to, the Tyrrhena Patera flank flow unit. This observation and the continuation of many of these ridges into the Noachian highlands as thrust fault scarps suggest formation of NE striking thrust faults no later than the late Noachian/early Hesperian. The NW striking wrinkle ridges, forming after the emplacement of the late Hesperian/early Amazonian Tyrrhena Patera deposit, imply geologically recent thrust faulting. The combination of NE and NW structural events implies a stress state rotation in Hesperia Planum of about 90° between the late Noachian and early Amazonian.

Citation: Goudy, C. L., R. A. Schultz, and T. K. P. Gregg (2005), Coulomb stress changes in Hesperia Planum, Mars, reveal regional thrust fault reactivation, *J. Geophys. Res.*, *110*, E10005, doi:10.1029/2004JE002293.

1. Introduction

[2] Mare-type wrinkle ridges are linear to arcuate asymmetric topographic highs, consisting of a broad arch topped by a crenulated ridge, where the entire structure is the "ridge" and crenulated portion is the "wrinkle" [*Strom*, 1972; *Watters*, 1988]. The origin of this type of planetary structure, commonly observed on the Moon [e.g., *Lucchitta*, 1977; *Sharpton and Head*, 1988], Mars [e.g., *Chicarro et al.*, 1985; *Plescia*, 1991; *Watters and Robinson*, 1997], Mercury [e.g., *Strom et al.*, 1975] and Venus [e.g., *Bilotti and Suppe*, 1999; *Hansen*, 2000], is an anticlinal fold that begins and grows as a result of slip on a blind-thrust fault at depth [*Schultz*, 2000]. The surface morphology of particular wrinkle ridges depends on factors related to the main thrust fault, such as fault-dip angle, fault-dip direction, fault length, and displacement distribution; with additional factors being geometry of folding, crustal stratification, interface strength, and degree of strain localization [*Mangold et al.*, 1998; *Schultz*, 2000; *Okubo and Schultz*, 2003]. Backthrusts form as a result of strain localization due to bedding-plane slip and flexural-slip folding. Wrinkles are the surface expression of backthrusts. Topographic offset across wrinkle ridges is consistent with blind thrusts that do not flatten into a décollement at depth [*Schultz*, 2000; *Okubo and Schultz*, 2004].

[3] One of the classic areas for Martian wrinkle ridges is the Lunae Planum region, an extensive area of ridged plains in the Tharsis province [*Watters and Maxwell*, 1986]. The wrinkle ridges in this area display a distinctive circumferential pattern around the Tharsis Plateau and are generally distributed in a broad, discontinuous band [*Wise et al.*, 1979; *Watters and Maxwell*, 1986; *Watters*, 1993]. The type locality for ridged plains on Mars is the Hesperia Planum region (Figure 1), situated northeast of Hellas Planitia [*Scott and Tanaka*, 1986; *Greeley and Guest*, 1987; *Watters and Chadwick*, 1989]. In contrast to Lunae Planum and other ridged plains on Mars, the wrinkle ridges in Hesperia Planum are well developed in two main directions: NW and NE [*Watters and Chadwick*, 1989; *Watters*, 1993; *Goudy and Gregg*, 2001, 2002]. The curiously orthogonal

0148-0227/05/2004JE002293$09.00

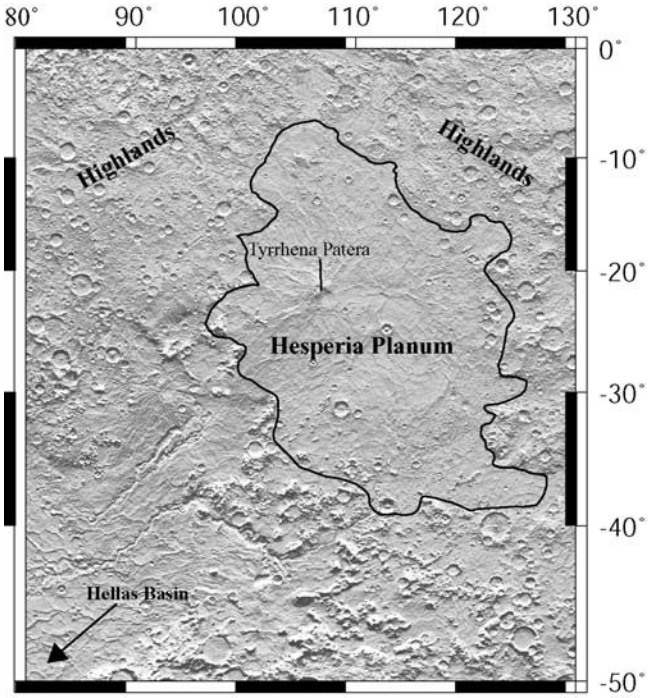

Figure 1. MOLA DEM (200 pixels/degree) showing location and boundary of Hesperia Planum, northeast of Hellas Basin (direction indicated by the arrow), Tyrrhena Patera in the west, and the surrounding Noachian highlands. The boundary between Hesperia Planum and the surrounding highlands is marked by a change in topography and surface geology. Mapped after *Greeley and Guest* [1987].

pattern in this area provides a unique opportunity to explore temporal and kinematic relationships between two populations of wrinkle ridges.

[4] On Earth, fault slip has been shown to cause changes in the local stress field and can trigger earthquakes on neighboring faults [e.g., *Freed and Lin*, 1998; *Anderson and Johnson*, 1999; *Stein*, 1999; *Ziv and Rubin*, 2000; *Lin and Stein*, 2004]. Recent studies show that stress changes as small as 0.01 MPa may trigger movement along a nearby fault [*Reasenberg and Simpson*, 1992; *Stein et al.*, 1992; *King et al.*, 1994; *Fialko and Simmons*, 2001]. *Freed and Lin* [1998] and *Lin and Stein* [2004] showed that thrust-related earthquakes cause a coseismic increase in Coulomb stress along antithetic lobes normal to the slip plane. The lateral extent of the lobes depends primarily on fault dip and slip magnitude [*Freed and Lin*, 1998].

[5] In this paper, we demonstrate that the two sets of wrinkle ridges in Hesperia Planum are temporally distinct. Within each set the wrinkle ridges are morphologically similar, but the comparison between sets reveals an unequal development of the NE striking wrinkle ridges, which indicates a more complex formational sequence than previously concluded. We show that the NW striking set of subwrinkle ridge thrust faults reactivates older faults, which subsequently localize wrinkle ridges on top of the Hesperia Planum deposit in two directions, under the same (Amazonian) remote stress state. The formational sequence is shown to occur in three stages (Figure 2): the older (NE) thrust faults form prior to the deposition of Hesperia Planum and are buried, secondly the stress state changes and wrinkle ridges begin to form in the NW striking direction. With the formation of the NW striking wrinkle ridges the buried NE thrust faults are reactivated as wrinkle ridges on top of the Hesperia Planum deposit. The concept of thrust-fault reactivation in the Hesperia Planum region implies a stress state rotation of 90° between the formation of the older, late Noachian structures, and younger, post late Hesperian/early Amazonian wrinkle ridges.

2. Spatial and Temporal Distribution of Wrinkle Ridges in Hesperia Planum

2.1. Relative Timing and Age Relationships

[6] Relative ages of the ridged plains of Hesperia Planum, using impact crater densities, were obtained from *Tanaka*'s [1986] method [*Greeley and Guest*, 1987; *Crown et al.*, 1992; *Tanaka and Leonard*, 1995; *Gregg et al.*, 1998; *Mangold et al.*, 2000; *Leonard and Tanaka*, 2001; *Mest and Crown*, 2001]. In general, these studies agree that the ridged plains material is early Hesperian [*Tanaka*, 1986; *Greeley and Guest*, 1987; *Mangold et al.*, 2000; *Leonard and Tanaka*, 2001; *Mest and Crown*, 2001], with younger ages (late Hesperian to early Amazonian) in the southern part of Hesperia Planum [*Mangold et al.*, 2000], and a Noachian age for the surrounding highlands. The volcanic flank flow unit of Tyrrhena Patera [*Greeley and Crown*, 1990] in southwestern Hesperia Planum (Figure 1) is late Hesperian to early Amazonian in age [*Crown et al.*, 1992; *Gregg et al.*, 1998].

[7] Numerous studies have been conducted with Viking Orbiter data to determine the relative ages of each set of wrinkle ridges in Hesperia Planum [*Chadwick*, 1991; *Porter et al.*, 1991; *Watters*, 1993; *Mangold et al.*, 2000; *Goudy and Gregg*, 2002], although no agreement had been reached prior to this study. Within the Tyrrhena Patera flank flow unit, two wrinkle ridge sets have been identified that date from late Hesperian to early Amazonian [*Crown et al.*, 1992; *Gregg et al.*, 1998]. Using cross-cutting relationships *Porter et al.* [1991] determined that within the Tyrrhena Patera flank flow unit the NW striking wrinkle ridges are younger than the flank flow unit and the NE striking wrinkle ridges, while the NE striking wrinkle ridges are older than, or temporally inseparable from, the flank flow unit (late Hesperian/early Amazonian).

[8] In contrast to the timing events observed in southwestern Hesperia Planum by *Porter et al.* [1991], *Chadwick* [1991] found no consistent relationship when he examined 60 wrinkle-ridge intersections in eastern Hesperia Planum. Observations reported by *Mangold et al.* [2000] show that most of the ridges in the NE striking direction are older, but some of the NE striking ridges appear deformed by NW striking wrinkle ridges. They concluded that both sets of wrinkle ridges in Hesperia Planum formed contemporaneously. *Goudy and Gregg* [2002] examined intersections using cross-cutting relationships and made the same observations (i.e., NE striking ridges deformed by NW striking ridges and NW striking ridges deformed by NE striking ridges) as *Mangold et al.* [2000]; however, *Goudy and Gregg* [2002] concluded that the NW striking wrinkle ridges were older. This inconsistent pattern is explained

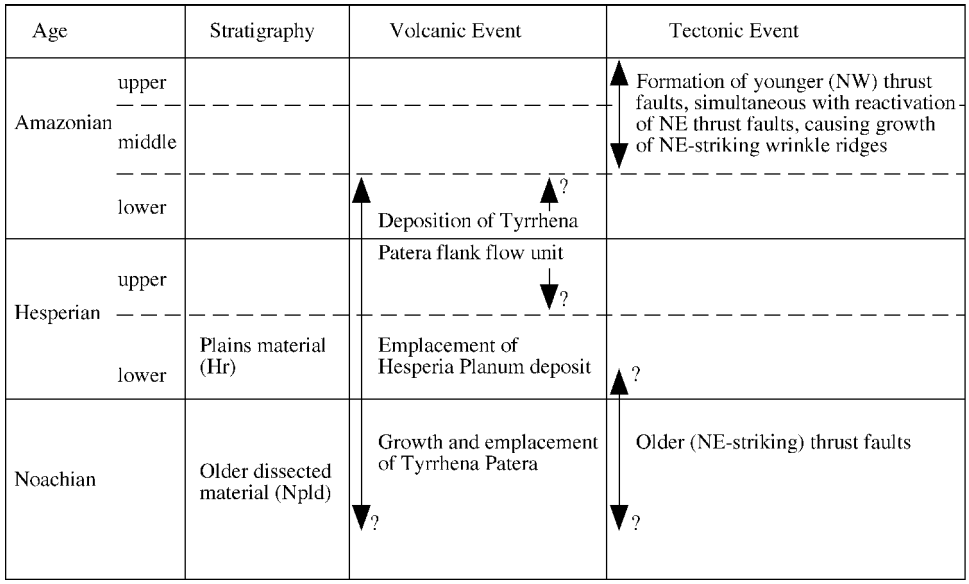

Figure 2. Relative sequence of events in Hesperia Planum.

partly by a combination of complex thrust fault geometry at the intersection of two wrinkle ridges [e.g., *Twiss and Moores*, 1992; *Rigo et al.*, 2004], and that the observations were made with Viking Orbiter images.

2.2. Reevaluation of Wrinkle Ridge Timing

[9] Wrinkle ridges in Hesperia Planum occur in an orthogonal pattern with ridges trending in the NE and NW striking directions [e.g., *Watters and Chadwick*, 1989; *Watters*, 1993; *Goudy*, 2002]. *Goudy* [2002] mapped all linear to sublinear wrinkle ridges visible in the Viking Orbiter images in Hesperia Planum, with Hesperia Planum boundaries mapped after *Greeley and Guest* [1987] (Figure 1), to statistically determine wrinkle-ridge orientations. Each linear to sublinear wrinkle ridge was weighted according to length and analyzed according to strike direction. Two populations of wrinkle ridges were found with mean orientations of $53 \pm 25°$ and $141 \pm 32°$ in the NE and NW striking directions, respectively [*Goudy*, 2002]. The next step was to determine the relative timing between wrinkle-ridge sets to understand the formational mechanism and the evolution of Hesperia Planum.

[10] Digital elevation models of Hesperia Planum were created for this study with a resolution of 200 pixels per degree from high-resolution Mars Orbiter Laser Altimeter (MOLA) data (Figure 3) (see *Okubo et al.* [2004] for method and discussion). We used these to reexamine the timing of wrinkle ridges in Hesperia Planum. MOLA topography allows us to identify wrinkle ridges and the subjacent thrust faults more definitively than is possible using the Viking Orbiter images, and cover a larger area than the Mars Orbiter Camera (MOC) images, which enables us to evaluate timing relationships, in detail, among wrinkle-ridge sets over a large area. A digital elevation model (DEM) of eastern Hesperia Planum (Figure 3) reveals a consistent relationship of the NE striking wrinkle ridges being topographically lower than the NW striking wrinkle ridges. The NE striking wrinkle ridges occur adjacent to the NW striking wrinkle ridges and become more subdued with distance from the intersection, which suggests that the NE striking wrinkle ridges are older thrust faults that were reactivated by the NW striking wrinkle ridges. This same timing relationships (i.e., cross-cutting relationships) are observed in the Thermal Emissions Imaging System (THEMIS) images (e.g., I08011003N, I08017011N); however, because wrinkle ridges are defined on the basis of topographic morphology, the relationship is better seen in the DEMs. The NW striking wrinkle ridges consistently override the NE striking wrinkle ridges and are thus temporally distinct on the basis of this cross-cutting relationship. In previous studies these timing relationships were not readily apparent (Figures 3b and 3c) [e.g., *Chadwick*, 1991; *Porter et al.*, 1991; *Goudy and Gregg*, 2002]. Figure 3b shows a clear example in the DEM where the NW striking ridge overrides the NE striking ridge and is younger on the basis of this relationship. The opposite relationship is suggested in the Viking Orbiter image, where the NE striking ridge appears to override the NW striking wrinkle ridges. This opposite relationship is due to the unfavorable illumination geometry in the Viking Orbiter data, which is from the northwest. The illumination geometry accentuates shadows associated with NE striking wrinkle ridges, which complicates cross-cutting relationship interpretations. MOC images have a small areal coverage in each image, so regional analysis is not possible from this data set.

2.3. Wrinkle Ridge Topography

[11] Timing and morphologic observations of each set of wrinkle ridges are clearly demonstrated in Figure 3. The individual wrinkle-ridge topography is consistent within each set, but differs between the two sets, i.e., shallower

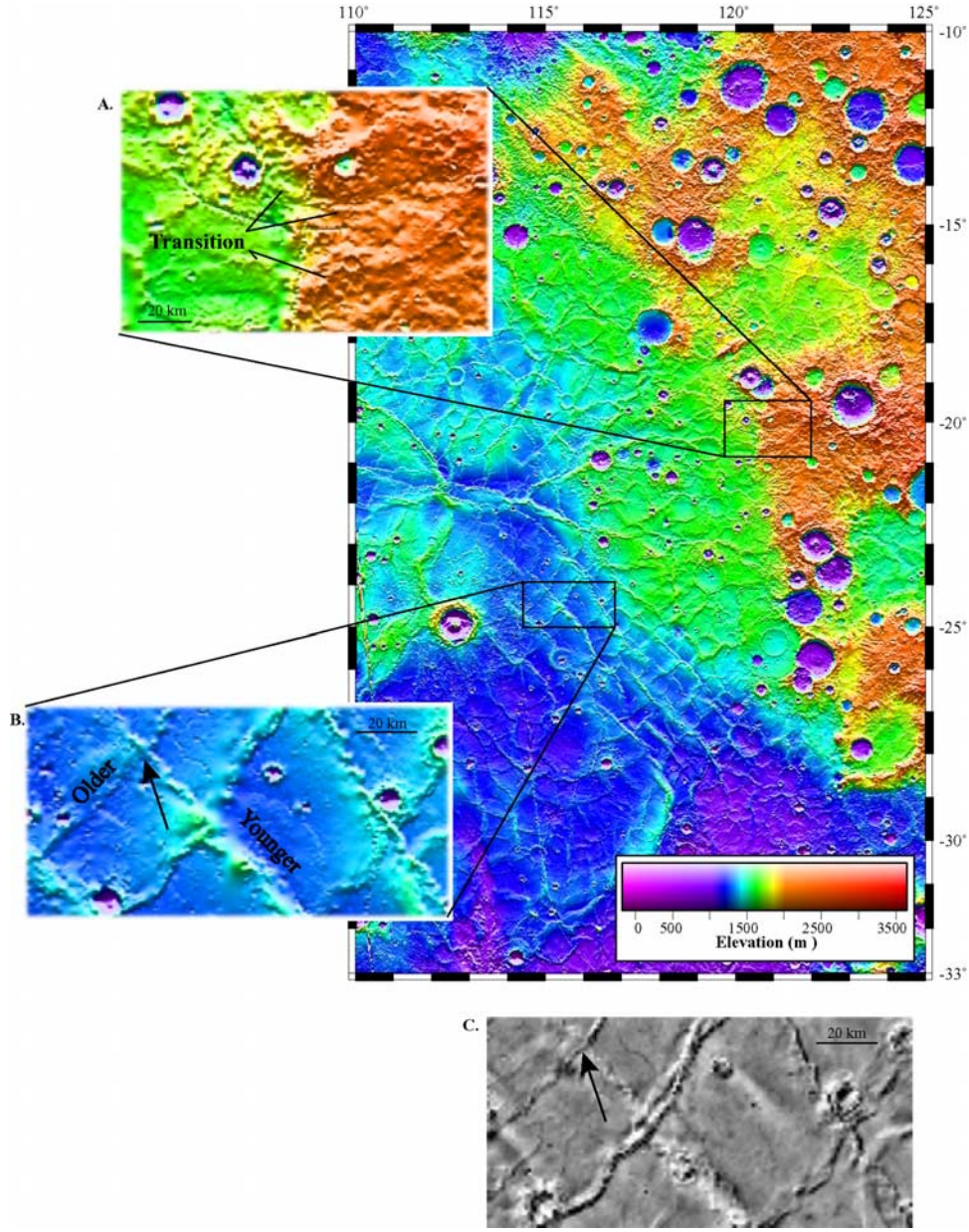

Figure 3. MOLA DEM (200 pixels/degree) of the eastern part of Hesperia Planum showing the consistent relationship of topographically subdued NE striking wrinkle ridges and more prominent NW striking wrinkle ridges. (a) Several wrinkle ridges in Hesperia Planum make the transition to the highlands as thrust fault scarps as indicated by the arrows. (b) An enlarged DEM of wrinkle ridges showing the clear cross-cutting relationship of the NE and NW sets of wrinkle ridges. The vergence of the wrinkle ridges is toward the SE for the NE striking set and SW for the NW striking set, which is interpreted as thrusts dipping in the SE and SW directions. (c) Viking Orbiter image of the same area shown in Figure 3b (http://pdsmaps.wr.usgs.gov). The arrows in both Figures 3b and 3c show an example of a cross-cutting relationship that can be misinterpreted using only the Viking Orbiter data due to illumination geometry. In Figures 3a and 3b, illumination is from the north, and in Figure 3c, illumination is from the northwest.

topography in the NE striking wrinkle ridges (Figure 3). The broad rise of each wrinkle ridge in the NW striking direction is consistently on the SW limb. This can be seen on the DEM (Figure 3) as well as in individual MOLA topographic profiles and is interpreted as a blind thrust dipping toward the SW [see *Schultz*, 2000; *Okubo and Schultz*, 2003, 2004; and references therein]. The NW striking wrinkle ridges are more continuous than the NE striking ridges, where many ridges extend from the intersection of the NW striking ridge to tens of kilometers and

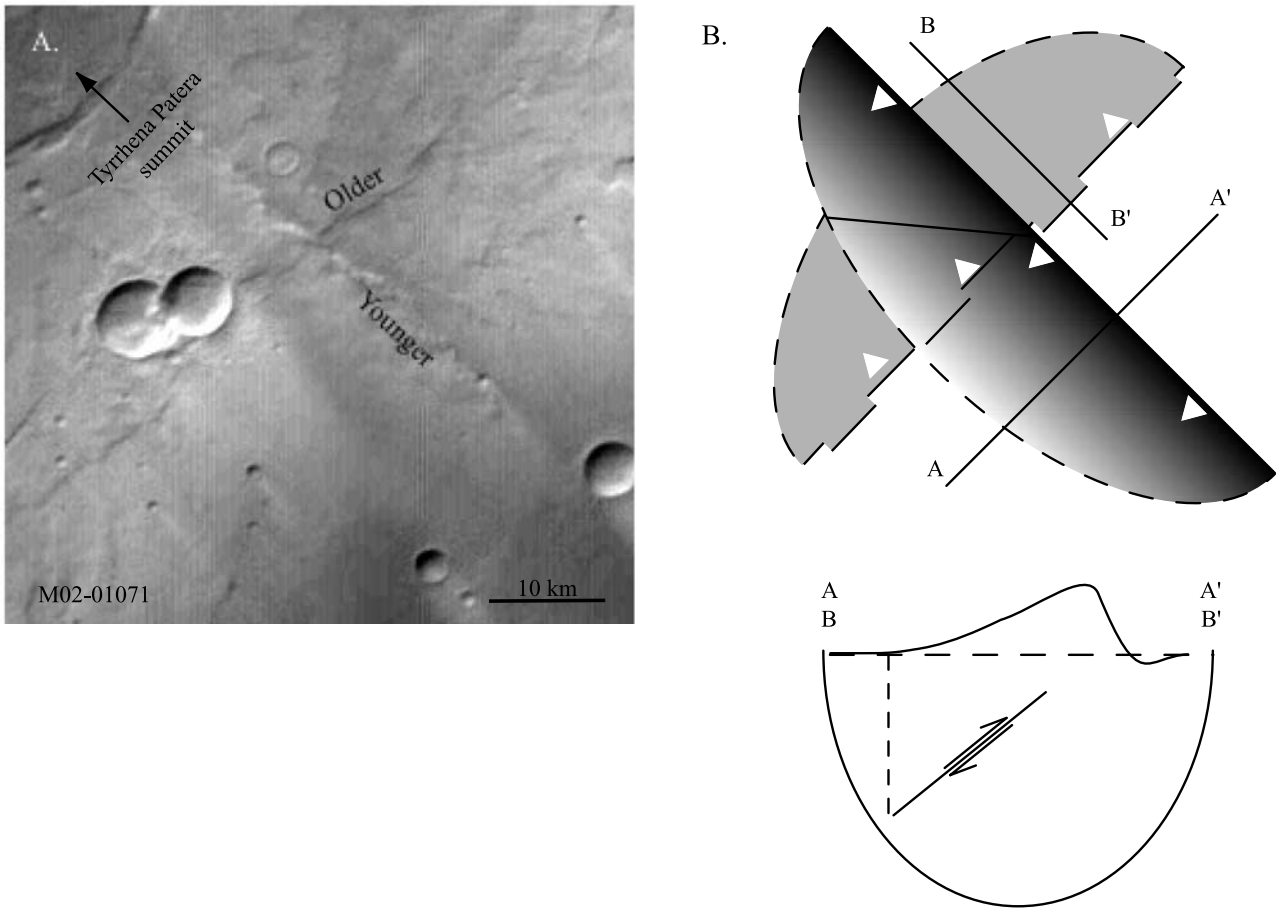

Figure 4. (a) A NW striking wrinkle ridge overrides both the Tyrrhena Patera deposit and the NE striking wrinkle ridge (image centered at approximately 21.6°S, 106.5°E). The NE striking wrinkle ridge dies out approximately 30 km from the NW striking wrinkle ridge, which indicates slip along the fault plane was triggered by thrust faulting beneath the NW striking wrinkle ridge (MOC image from http://www.msss.com, M02-01071). (b) The source fault (beneath the NW striking wrinkle ridge) is continuous and is shown in black. The receiver fault (the wrinkle ridge is above the reactivated NE striking thrust fault) is shown in gray and displays an echelon pattern which dies out with distance from the NW striking wrinkle ridge.

then disappear as their relief diminishes to zero (Figures 3 and 4). In contrast, the NE striking wrinkle ridges dip in the NW direction, because the broad rise is on the NW side of the wrinkle ridges (Figure 3).

[12] There is a significant and systematic morphologic difference between the two sets of wrinkle ridges (Table 1). The NE striking wrinkle ridges show an echelon pattern, are shorter than NW striking wrinkle ridges, only occur adjacent to NW striking wrinkle ridges (Figure 3), and the topography of some NE striking ridges becomes subdued with distance from the NW striking ridge (Figures 3 and 4). Many NE striking wrinkle ridges parallel scarps, interpreted to be thrust fault scarps, outside of Hesperia Planum in the Noachian highlands. In a few places in the eastern part of Hesperia Planum NE striking wrinkle ridges are observed extending into the Noachian highlands as thrust fault scarps (Figure 3). The thrust fault scarps in the highlands are coincident with late Noachian to early Hesperian faulting [*Watters*, 2003a, 2003b]. These observations demonstrate that the two sets of wrinkle ridges are not equally developed as might be expected if formation occurred by two temporally distinct thrust faulting/wrinkle ridge building events [e.g., *Chadwick*, 1991] (Figure 4).

[13] There are two alternative scenarios to explain the wrinkle ridge pattern in Hesperia Planum. The first is that the wrinkle ridges are sequential with the NW striking wrinkle ridges being older than the NE striking wrinkle ridges, with the propagation of the NE striking wrinkle ridge producing the wrinkle on the top of the NW striking wrinkle ridge. If this were the case, we would expect continuity of both sets of wrinkle ridges. Instead, we see an echelon pattern in the NE striking wrinkle ridges, with NE striking wrinkle ridges only occurring adjacent to NE striking ridges. In the second scenario the two sets of wrinkle ridges formed contemporaneously [*Mangold et al.*, 2000]. This situation requires a complicated horizontal stress state, which allows formation of orthogonal structures where both horizontal principal stresses are nearly equal. In this situation we would expect both wrinkle ridge sets to show a continuous pattern and cross-cutting relationships would be inconsistent in the DEMs. We find that the only the NW striking wrinkle ridges have a continuous pattern

Table 1. Differences in Wrinkle Ridge Patterns and Morphology Observed in MOLA DEMs

	NW Striking Wrinkle Ridges (Younger)	NE Striking Wrinkle Ridges (Older)
Map pattern	continuous	echelon
Spacing	periodically spaced	periodically spaced, but occur adjacent to younger (NE striking) ridges
Topography	constant topography along strike	subdued topography that diminishes with distance from the intersection
Location	largely restricted to Hesperia Planum	parallel thrust fault scarps in the highlands

and timing relationships are consistent in the DEMs (Table 1). Therefore we investigate the possibility of NW striking wrinkle ridges reactivating preexisting buried Noachian thrust faults, following a stress state rotation between the late Noachian to the early Amazonian.

3. Methods

[14] The observations of the two wrinkle-ridge sets made from the DEMs, i.e., timing and morphological differences, and the continuation of wrinkle ridges into the highlands as thrust fault scarps, suggest that the orthogonal pattern in Hesperia Planum reduces to a fault reactivation, i.e., triggered slip, problem. For terrestrial data sets, the standard approach to fault reactivation problems involves calculating the change in Coulomb failure stress induced on an older fault by slip on a younger fault, which we follow after *King et al.* [1994] [e.g., *Freed and Lin*, 1998; *Harris*, 1998; *Harris and Simpson*, 1998; *Stein*, 1999; *Ziv and Rubin*, 2000; *Wilkins and Schultz*, 2003; *Lin and Stein*, 2004].

[15] Fault reactivation of NE striking wrinkle ridges is examined here by calculating the change in Coulomb failure stress (ΔCFS) along a receiver fault (the older thrust faults) oriented perpendicular to a source fault (beneath the younger wrinkle ridges) in the NW striking direction using the dislocation program COULOMB [*Toda et al.*, 1998]. Since many ridged plains units are interpreted to result from flood volcanism and lunar wrinkle ridges formed in material of basaltic composition [*Greeley et al.*, 1977; *Scott and Carr*, 1978; *Scott and Tanaka*, 1986], we tested our model assuming a basaltic stratigraphy. A friable material, tuff, was also investigated, because the flanks of Tyrrhena Patera are dissected by radial channels and the material surrounding Tyrhenna Patera is characterized by shallow slopes (<2°), both suggesting a pyroclastic origin [*Gregg et al.*, 2002].

[16] The Coulomb failure criterion is given by

$$\Delta CFS = \Delta\tau - \mu'\Delta\sigma_n, \tag{1}$$

where $\Delta\tau$ is the change in shear stress in the slip direction and $\Delta\sigma_n$ is the change in normal stress along the receiver-fault plane. The apparent coefficient of maximum static friction (μ') is taken to be 0.4, and implicitly accounts for changes in pore pressure that arise from changes in normal stress, bulk moduli and porosity of the fault rock [e.g., *Harris*, 1998; *Harris and Simpson*, 1998; *Freed and Lin*, 1998]. The apparent coefficient of maximum static friction is determined for rock by analogy to Skempton's coefficient, B, which ranges between 0 and 1, defined as [*Harris*, 1998; *Beeler et al.*, 2001],

$$\mu' = \mu(1 - B), \tag{2}$$

where μ, the coefficient of friction, is 0.6 [*Harris*, 1998]. Therefore, when $B = 0.333$ [see *Harris*, 1998; *Beeler et al.*, 2001],

$$0.4 = 0.6(1 - B). \tag{3}$$

Changes in pore pressure and dynamic friction during faulting may change μ'; however, modest variations in this parameter would not significantly alter the results [e.g., *King et al.*, 1994; *Schultz and Lin*, 2001]. Use of the Coulomb frictional sliding criterion on Mars is a special case of rate-and-state friction due to the lack of data on temporally dependent changes in slip rate and fault-related friction [*Gomberg et al.*, 1998]. In this approach μ' is independent of the magnitude of stress changes and time; it behaves as a material constant [*Simpson and Reasenberg*, 1994; *Beeler et al.*, 2000], and appears to be representative of in situ conditions on Mars where a mechanically weak layer is present [*Okubo and Schultz*, 2004].

[17] Elliptical slip distributions were designated along strike of the source fault, with maximum values defined from

$$D_{\max} = \gamma L, \tag{4}$$

where γ is approximately 0.001 [*Schultz and Fossen*, 2002; *Wilkins et al.*, 2002; *Wilkins and Schultz*, 2003], and L is the length of the thrust fault beneath the wrinkle ridge, which is typically about 100 km [see *Goudy*, 2002; *Goudy and Gregg*, 2002].

[18] A stress field appropriate for Coulomb frictional sliding in a thrust-faulting regime is adopted for all calculations [*King et al.*, 1994; *Toda et al.*, 1998]. This stress state is defined using horizontal σ_1 and vertical σ_3 stresses

$$\sigma_1 = q'\sigma_3 + \sigma_c^*, \tag{5}$$

where q' is the bulk friction parameter [*Jaeger and Cook*, 1979],

$$q' = \left(\sqrt{\mu'^2 + 1} + \mu'\right)^2, \tag{6}$$

$$\sigma_3 = \rho g z, \tag{7}$$

$$\sigma_c^* = \sqrt{s\sigma_c} \tag{8}$$

[*Schultz*, 2005], and ρ is dry rock density, taken to be 2700 kg/m^3 for basalt and 2100 kg/m^3 for tuff, g is gravity 3.72 m/s^2, and z is depth. Compressive strength of the rock mass, σ_c^*, is a function of the compressive strength of the

intact rock material (σ_c), approximately 210 MPa for basalt and 18 MPa for tuff [*Goodman*, 1989; *Schultz*, 1995]. Parameter s, associated with the Hoek-Brown failure criterion, reflects the degree of interlocking and fracturing of the rock, given by

$$s = \exp^{\frac{RMR-100}{9}}, \tag{9}$$

where rock mass rating (RMR) is taken to be 55 for both basalt and tuff, on the basis of terrestrial analogs [*Bieniawski*, 1989; *Schultz*, 1993]. Wrinkle ridges in Hesperia Planum, in the NW direction, are on the order of 100 km long [*Goudy*, 2002]; therefore, at the time of formation, and in our model, wrinkle ridges are taken to be in plane strain with vertical deformation resulting from stress from two horizontal components (σ_1 and σ_2). The intermediate principal stress, parallel to the wrinkle ridge, σ_2, is given by

$$\sigma_2 = \nu(\sigma_1 + \sigma_3), \tag{10}$$

where Poisson's ratio, ν, is 0.25. Young's modulus for the rock mass (E^*) is given by [*Bieniawski*, 1989]

$$E^* = [(2\mathrm{RMR}) - 100] = 10(\mathrm{GPa}), \tag{11}$$

and the shear modulus, G, is calculated using

$$G = \frac{E^*}{2(1+\mu)} = 4(\mathrm{GPa}). \tag{12}$$

[19] The orientation of the optimum slip plane of the subjacent thrust fault, θ_f, was determined using

$$\theta_f = 90^\circ - \tan^{-1}\frac{1/\mu'}{2}. \tag{13}$$

This is the angle between σ_1 and the normal to the optimum slip plane. Using $\mu' = 0.4$, the thrust faults should dip at 36 ± 2°. This optimal slip angle is used for both the source fault and the receiver fault. Many wrinkle ridges extend into the highland material as thrust-fault scarps, which reflect regional deformation (beyond the site of Hesperia Planum) during the late Noachian to early Hesperian (Figure 3) [*Schultz*, 2000; *Watters*, 1993, 2003a, 2003b]. These fault scarps dip at approximately 30° [*Schultz and Watters*, 2001], which is close to the estimate calculated in this study for the optimal angle of thrust fault slip, 36° [*Byerlee*, 1968; *Watters*, 1993; *Sibson*, 1994].

[20] The relative dip directions with respect to the source fault and receiver fault were obtained from the DEM of Hesperia Planum (Figure 3). The source fault is set along the horizontal x axis and dips toward the negative y direction. The receiver fault is set along the vertical y axis and dips toward the negative x direction (Figure 5a). Coulomb stress change calculations on the plane of the receiver fault are made for a 150 element grid. Coulomb stress changes and the associated rake, or direction of slip, are resolved on the surface of the receiver fault [*Jaeger and Cook*, 1979; *Sibson*, 1994; *Bruhn and Schultz*, 1996].

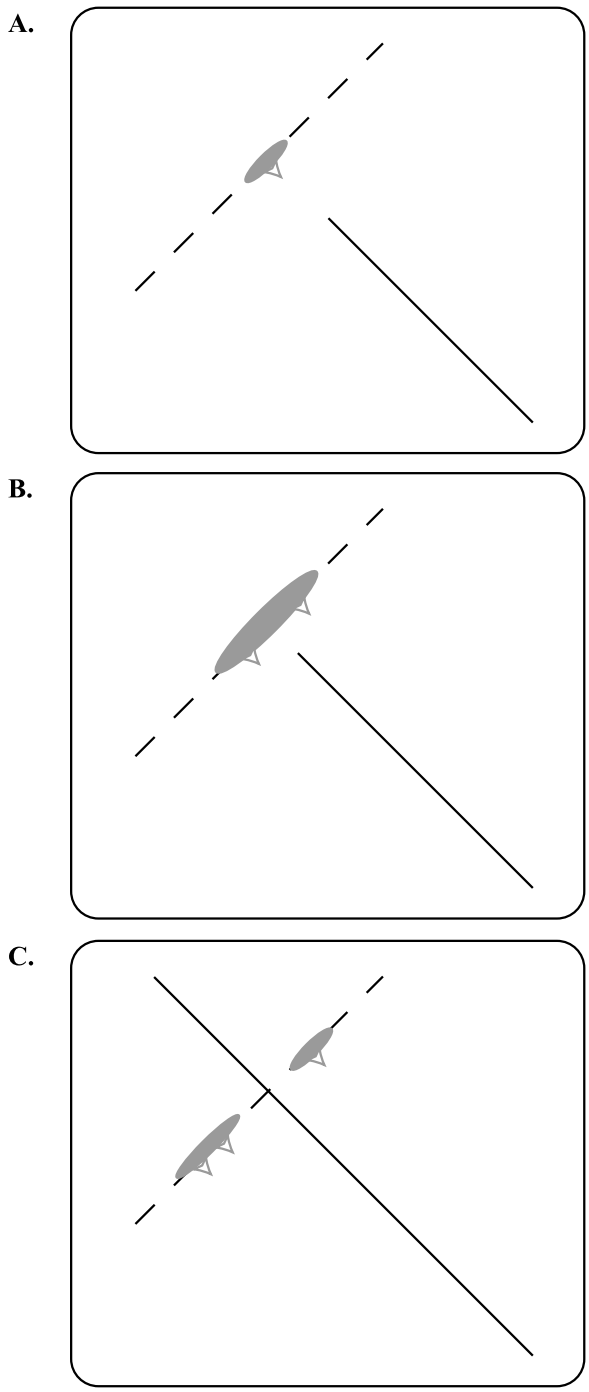

Figure 5. As the source fault (indicated by the solid line) approaches the receiver fault (dashed line) (a) reactivation along the receiver fault (shaded, with thrust symbol) is triggered adjacent to the source fault, (b) the reactivated area spreads along the receiver fault as the source fault propagates toward the receiver fault, and (c) reactivation becomes hindered at the intersection of the two faults but continues to spread along the receiver fault with distance from the intersection.

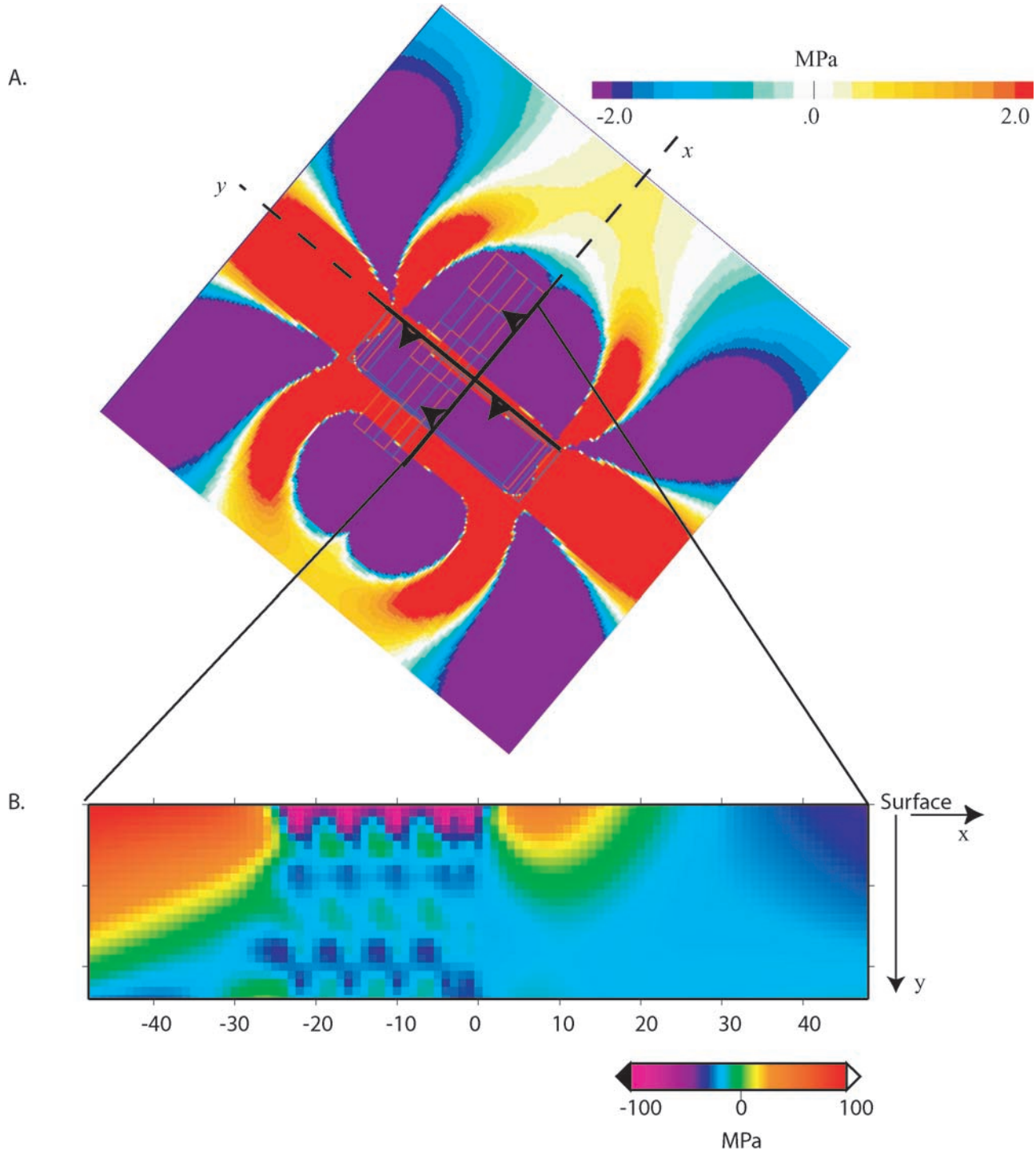

Figure 6. Changes in Coulomb failure stress (ΔCFS) along the fault planes. (a) Source fault intersecting a receiver fault in map view where a positive ΔCFS is shown in red and a negative ΔCFS is shown in blue. The receiver fault (dashed) is aligned along the *x* axis and is separated into 150 elements along the *y* axis. The source fault is aligned along the *y* axis. (b) ΔCFS along receiver fault plane for basalt where the source fault is at the intersection. Changes in Coulomb failure stress vary with depth and distance along the receiver fault and are dependent upon the angle of intersection of the source fault.

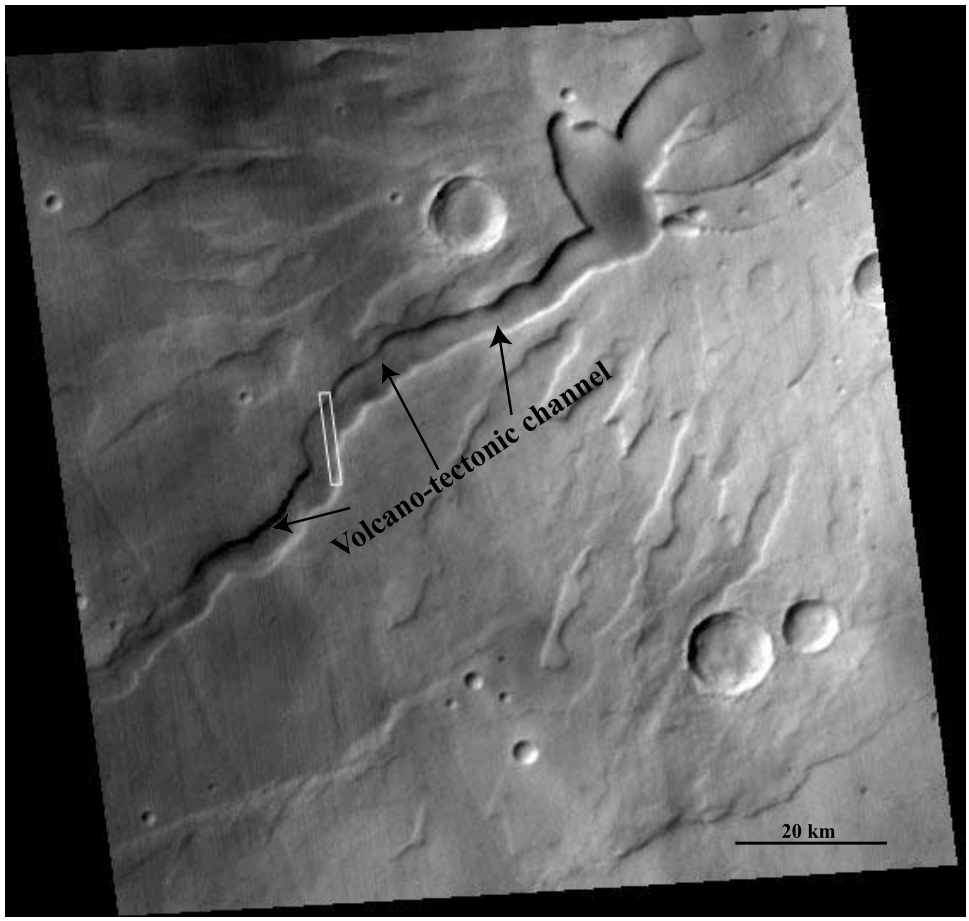

Figure 7. MOC wide-angle image showing a volcano-tectonic channel that is radial to the summit caldera of Tyrrhena Patera (http://www.msss.com, M02-04725).

Increased Coulomb failure stress change promotes frictional sliding on the receiver fault (positive ΔCFS), and decreased values hinder slip along it (negative ΔCFS) [*Gross and Kisslinger*, 1994; *Harris and Simpson*, 1998]. Positive ΔCFS as small as 0.01 MPa increases the likelihood of triggered slip [*Reasenberg and Simpson*, 1992]. Because changes in the local stress state around faults are spatially variable, ΔCFS is calculated using equation (1) in a three-dimensional homogeneous and isotropic linear-elastic half-space [*Pollard and Segall*, 1987; *King et al.*, 1994; *Toda et al.*, 1998]. The rake along each receiver fault is determined from a combination of the induced stress field and the regional stress field, where displacement occurs in the direction of the maximum shear stress along the surface of resolved stresses.

4. Results

[21] Cumulative Coulomb stress changes along receiver faults in both basalt and tuff are calculated as a source fault approaches (Figure 5) and after the source fault has intersected and propagated through the receiver fault (Figure 6). The changes in Coulomb failure stress vary with depth and, especially, distance along the receiver fault plane. The changes in Coulomb failure stress on the Martian surface are calculated in map view (Figure 6a), and show the source fault producing a positive change in Coulomb failure stress in front of and behind the source fault, in addition to positive changes along the receiver fault plane. Slip is triggered as the source fault propagates toward the receiver fault (Figure 5). At the intersection of the two faults, the receiver fault is locked there, and slip is promoted within tens of km from the intersection itself.

[22] In regions surrounding source faults, Coulomb stress changes predict failure in a thrust sense along pre-existing orthogonal faults, which is shown by a positive change in Coulomb failure stress (Figure 6). The associated rake shows thrust movement is triggered toward the intersection. Negative changes in Coulomb failure stress, associated with slip impedance, exist on the receiver fault in areas adjacent to the footwall of the source fault (Figure 6b). This indicates that the angle and direction that the source fault is dipping are critical to triggering slip along the receiver fault plane.

[23] Coulomb failure stress change for tuff is smaller than that for basalt when all other conditions are the same (i.e., an optimum fault dip angle of 34°, 100 m displacement, etc), because tuff has a lower density and compressive strength. The changes calculated for both basalt and tuff are cumulative changes in Coulomb failure stress throughout the entire reactivation history of this area, instead of a

single slip event. The calculations of changes in Coulomb failure stress for basalt range from −100 to 100 MPa, and for tuff this change is less, −50 to 50 MPa. This indicates that there is a smaller amount of Coulomb failure stress change necessary to produce the observed topography in tuff than in basalt, and slip may be triggered at greater distances from the source-fault in tuff than in basalt. In the area of Hesperia Planum the spacing between wrinkle ridges in the NE striking direction ranges from 16 to 32 km [*Goudy and Gregg*, 2002]. The stress-triggering results are compatible with this cross-strike spacing for either lithology.

5. Discussion

[24] The results of this study support two temporally distinct stress states and three deformational events (see Figure 2): (1) the formation of subsurface thrust faults in the NE striking direction, beneath the present Hesperia Planum in the late Noachian/early Hesperian; these thrust faults formed under a NW-SE compressive stress state; (2) a stress state rotation of about 90°; (3) formation of the NW striking thrust faults and their overlying wrinkle ridges, which caused the reactivation of the NE striking thrust faults to localize new wrinkle ridges on top of the Hesperian deposit in late Hesperian/early Amazonian time.

[25] *Porter et al.* [1991] found that the NE striking wrinkle ridges are older than the NW striking wrinkle ridges and older or temporally inseparable from the Tyrrhena Patera flank flow unit. *Greeley and Crown* [1990] suggest that the association of several large linear morphologically distinct volcano-tectonic channels and units composed of lavas indicates formation by tectonism and volcanism. The general trend of the radial volcano-tectonic channel is roughly parallel to the NE striking wrinkle ridges (Figure 7). The correlation of the formation of Tyrrhena Patera in the Noachian, the temporal relationship between wrinkle ridges and the flank flow unit of Tyrrhena Patera, and the orientation of the large volcano-tectonic channel suggest the NW striking wrinkle ridges reactivated thrust faults, which initially formed in the late Noachian/early Hesperian [*Greeley and Crown*, 1990; *Gregg et al.*, 1998, 2002]. Because pre-existing thrust faults in the NE striking direction represent the same deformational event that formed thrust fault scarps in the highlands, which we can infer from the transition of wrinkle ridges into the highlands as thrust fault scarps in eastern Hesperia Planum, then we place the age of the initial NE striking thrust faults to be of late Noachian to early Hesperian [*Watters*, 2003a, 2003b], which is in agreement with the cross-cutting relationships observed near Tyrrhena Patera [*Porter et al.*, 1991]. This implies that models or causes of northeast-trending faults, e.g., in association with the crustal dichotomy [*Watters*, 2003a, 2003b], would apply only to the NE striking thrust faults in Hesperia Planum, prior to their reactivation.

[26] The younger wrinkle ridges formed later than the Tyrrhena Patera flank flow unit [*Gregg et al.*, 1998] and later than the NE striking thrust faults. Therefore the most recent of these events is the formation of the NW striking wrinkle ridges and reactivation of the NE striking thrust faults in the late Hesperian to early Amazonian, which implies geologically recent thrust fault tectonism in this area of eastern Mars.

[27] Fault dip on each set of wrinkle ridges is consistent within each set of wrinkle ridges. The formation of the NE striking thrust faults occurring in the Noachian and the NW striking wrinkle ridges not forming until after the late Hesperian to early Amazonian may indicate a change in the thermal state of the lithosphere that accompanied a stress state rotation [*Montési and Zuber*, 2003]. A detailed analysis of wrinkle ridge spacing is needed to assess this hypothesis.

6. Conclusions

[28] The observations made in the DEMs, i.e., NE striking wrinkle ridges having a consistently subdued topography compared to the NW striking wrinkle ridges, the echelon pattern of NE striking wrinkle ridges, the extension of wrinkle ridges into the highlands as late Noachian/early Hesperian thrust fault scarps, and the existence of NE striking ridges only in proximity to NW striking ridges, are consistent with, and best explained by, fault reactivation. The results of the stress-triggering investigation in this study show that fault reactivation is likely to have occurred along the older receiver fault, from movement along the younger source fault at distances given by wrinkle-ridge spacing in Hesperia Planum. The associations of NE striking wrinkle ridges to the flank flow unit and the volcano-tectonic channel of Tyrrhena Patera, and the continuation of these ridges into the highlands as thrust fault scarps suggest that this older set of thrust faults formed no later than the late Noachian/early Hesperian. The NE striking thrust faults were later reactivated to form wrinkle ridges by the thrust faults beneath NW striking wrinkle ridges in the late Hesperian/early Amazonian.

[29] **Acknowledgments.** This work was supported in part by NASA's Planetary Geology and Geophysics Program and the Mars Data Analysis Program (grants to R. A. Schultz). We would also like to thank D. A. Crown, R. A. Harris, and L. G. Montési for their useful and thorough comments that sharpened the final paper.

References

Anderson, G., and H. Johnson (1999), A new statistical test for static stress triggering: Application to the 1987 Superstition Hills earthquake, *J. Geophys. Res.*, *104*, 20,153–20,168.

Beeler, N. M., R. W. Simpson, S. H. Hickman, and D. A. Lockner (2000), Pore fluid pressure, apparent friction, and Coulomb failure, *J. Geophys. Res.*, *105*, 25,533–25,542.

Beeler, N. M., S. H. Hickman, and T.-f. Wong (2001), Earthquake stress drop and laboratory-inferred interseismic strength recovery, *J. Geophys. Res.*, *106*, 30,701–30,713.

Bieniawski, Z. T. (1989), *Engineering Rock Mass Classifications: A Complete Manual for Engineers and Geologists in Mining, Civil and Petroleum Engineering*, John Wiley, Hoboken, N. J.

Bilotti, F., and J. Suppe (1999), The global distribution of wrinkle ridges on Venus, *Icarus*, *139*, 137–159.

Bruhn, R. L., and R. A. Schultz (1996), Geometry and slip distribution in normal fault systems: Implications for mechanics and fault-related hazards, *J. Geophys. Res.*, *101*, 3401–3412.

Byerlee, J. D. (1968), Brittle-ductile transition in rocks, *J. Geophys. Res.*, *73*, 4741–4750.

Chadwick, J. D. (1991), Superposition relations of wrinkle ridges in eastern Hesperia Planum, Mars (abstract), *Geol. Soc. Am. Abstr. Programs*, *23*, 277.

Chicarro, A. F., P. H. Schultz, and P. Masson (1985), Global and regional ridge patterns on Mars, *Icarus*, *50*, 129–139.

Crown, D. A., K. H. Price, and R. Greeley (1992), Geologic evolution of the east rim of the Hellas Basin, Mars, *Icarus*, *100*, 1–25.

Fialko, Y. M., and D. C. Simmons (2001), The complete (3-D) surface displacement field in the epicentral area of the 2000 M_w 7.1 Hector Mine earthquake, California, from space geodetic observations, *Geophys. Res. Lett.*, *28*, 3063–3066.

Freed, A. M., and J. Lin (1998), Time-dependent changes in failure stress following thrust earthquakes, *J. Geophys. Res.*, *103*, 24,393–24,409.

Gomberg, J., N. M. Beeler, M. L. Blanpied, and P. Bodin (1998), Earthquake triggering by transient and static deformations, *J. Geophys. Res.*, *103*, 24,411–24,426.

Goodman, R. E. (1989), *Introduction to Rock Mechanics*, 2nd ed., 562 pp., John Wiley, Hoboken, N. J.

Goudy, C. L. (2002), Wrinkle ridges of Hesperia Planum, Mars: Implications for the evolution of ridged plains, M.S. thesis, 130 pp., State Univ. of New York at Buffalo, Buffalo, N. Y.

Goudy, C. L., and T. K. P. Gregg (2001), Possible mechanisms of stress in Hesperia Planum, Mars: Digital analysis of mare-type wrinkle ridges, *Lunar Planet. Sci.*, *XXXII*, abstract 1393.

Goudy, C. L., and T. K. P. Gregg (2002), Insight to the evolution of wrinkle ridges in Hesperia Planum, Mars, *Lunar Planet. Sci.*, *XXXIII*, abstract 1135.

Greeley, R., and D. A. Crown (1990), Volcanic geology of Tyrrhena Patera, Mars, *J. Geophys. Res.*, *95*(B5), 7133–7149.

Greeley, R., and J. E. Guest (1987), Geologic map of the eastern equatorial region of Mars, *U.S. Geol. Surv. Misc. Invest. Ser., Map I-1802-B*.

Greeley, R., E. Theilig, J. E. Guest, M. H. Carr, H. Masursky, and J. A. Cutts (1977), Geology of Chryse Planitia, *J. Geophys. Res.*, *82*, 4039–4109.

Gregg, T. K. P., J. H. Fink, and R. W. Griffiths (1998), Formation of multiple fold generations on lava flow surfaces: Influence of strain rate, cooling rate, and lava composition, *J. Volcanol. Geotherm. Res.*, *80*, 281–292.

Gregg, T. K. P., D. A. Crown, and S. E. H. Sakimoto (2002), Volcanic evolution and erosion at Tyrrhena and Hadriaca Paterae, Mars, *Lunar Planet. Sci.*, *XXXIII*, abstract 1560.

Gross, S. J., and C. Kisslinger (1994), Tests of models of aftershock rate decay, *Bull. Seismol. Soc. Am.*, *84*, 1571–1579.

Hansen, V. L. (2000), Geologic mapping of tectonic planets, *Earth Planet. Sci. Lett.*, *176*, 527–542.

Harris, R. A. (1998), Introduction to special section: Stress triggers, stress shadows, and implications for seismic hazard, *J. Geophys. Res.*, *103*, 24,347–24,358.

Harris, R. A., and R. W. Simpson (1992), Changes in static stress on southern California faults after the 1992 Landers earthquake, *Nature*, *360*, 251–254.

Harris, R. A., and R. W. Simpson (1998), Suppression of large earthquakes by stress shadows: A comparison of Coulomb and rate-and-state failure, *J. Geophys. Res.*, *103*, 24,439–24,451.

Jaeger, J. C., and N. G. W. Cook (1979), *Fundamentals of Rock Mechanics*, 3rd ed., 593 pp., CRC Press, Boca Raton, Fla.

King, G. C. P., R. S. Stein, and J. Lin (1994), Static stress changes and the triggering of earthquakes, *Bull. Seismol. Soc. Am.*, *84*, 935–953.

Leonard, G. J., and K. L. Tanaka (2001), Geologic map of the Hellas region of Mars, *U.S. Geol. Surv. Geol. Invest. Ser., Map I-2694*.

Lin, J., and R. S. Stein (2004), Stress triggering in thrust and subduction earthquakes and stress interaction between the southern San Andreas and nearby thrust and strike-slip faults, *J. Geophys. Res.*, *109*, B02303, doi:10.1029/2003JB002607.

Lucchitta, B. K. (1977), Topography, structure, and mare ridges in southern Mare Imbrium and northern Oceanus Procellarum, *Proc. Lunar Sci. Conf. 13th*, 2691–2703.

Mangold, N., P. Allemand, and P. G. Thomas (1998), Wrinkle ridges of Mars: Structural analysis and evidence for shallow deformation by ice-rich décollments, *Planet. Space Sci.*, *46*, 345–356.

Mangold, N., P. Allemand, P. G. Thomas, and G. Vidal (2000), Chronology of compressional deformation on Mars: Evidence for a single and global origin, *Planet. Space Sci.*, *48*, 1201–1211.

Mest, S. C., and D. A. Crown (2001), Geology of the Reull Vallis region, Mars, *Icarus*, *153*, 89–110.

Montési, L. G. J., and M. T. Zuber (2003), Clues to the lithospheric structure of Mars from wrinkle ridge sets and localization instability, *J. Geophys. Res.*, *108*(E6), 5048, doi:10.1029/2002JE001974.

Okubo, C. H., and R. A. Schultz (2003), Thrust fault vergence directions on Mars: A foundation for investigating global-scale Tharsis-driven tectonics, *Geophys. Res. Lett.*, *30*(22), 2154, doi:10.1029/2003GL018664.

Okubo, C. H., and R. A. Schultz (2004), Mechanical stratigraphy in the western equatorial region of Mars based on thrust fault-related fold topography and implications for near-surface volatile reservoirs, *Geol. Soc. Am. Bull.*, *116*, 594–605.

Okubo, C. H., R. A. Schultz, and G. S. Stefanelli (2004), Gridding Mars Orbiter Laser Altimeter data with GMT: Effects of pixel size and interpolation methods on DEM integrity, *Comput. Geosci.*, *30*, 59–72.

Plescia, J. B. (1991), Wrinkle ridges in Lunae Planum, Mars: Implications for shortening and strain, *Geophys. Res. Lett.*, *18*, 913–916.

Pollard, D. D., and P. Segall (1987), Theoretical displacements and stresses near fractures in rock: With applications to faults, joints, veins, dikes, and solution surfaces, in *Fracture Mechanics of Rock*, edited by B. K. Atkinson, pp. 277–349, Elsevier, New York.

Porter, T. K., D. A. Crown, and R. Greeley (1991), Timing and formation of wrinkle ridges in the Tyrrhena Patera region of Mars, *Proc. Lunar Planet. Sci. Conf. 22nd*, 1085–1086.

Reasenberg, P. A., and R. W. Simpson (1992), Response of regional seismicity to the static stress change produced by the Loma Prieta earthquake, *Science*, *255*, 1687–1690.

Rigo, A., J. B. de Chabalier, B. Meyer, and R. Armijo (2004), The 1995 Kozani-Grevena (northern Greece) earthquake revisited: An improved faulting model from synthetic aperture radar interferometry, *Geophys. J. Int.*, *157*, doi:10.111/j.1365-246X.2004.02220.

Schultz, R. A. (1993), Brittle strength of basaltic rock masses with application to Venus, *J. Geophys. Res.*, *98*, 10,883–10,895.

Schultz, R. A. (1995), Gradients in extension and strain at the Valles Marineris rift, Mars, *Planet. Space Sci.*, *43*, 1561–1566.

Schultz, R. A. (2000), Localization of bedding plane slip and backthrust faults above blind thrust faults: Keys to wrinkle ridge structure, *J. Geophys. Res.*, *105*, 12,035–12,052.

Schultz, R. A. (2005), *Fractures in Rock: A Field Guide and Journey into Geologic Fracture Mechanics*, Oxford Univ. Press, New York, in press.

Schultz, R. A., and H. Fossen (2002), Displacement–length scaling in three dimensions: The importance of aspect ratio and application to deformation bands, *J. Struct. Geol.*, *24*, 1389–1411.

Schultz, R. A., and J. Lin (2001), Three-dimensional normal faulting models of the Valles Marineris, Mars, and geodynamic implications, *J. Geophys. Res.*, *106*(B8), 16,549–16,566.

Schultz, R. A., and T. R. Watters (2001), Forward mechanical modeling of the Amenthes Rupes thrust fault on Mars, *Geophys. Res. Lett.*, *28*, 4659–4662.

Scott, D. H., and H. Carr (1978), Geologic map of Mars, scale 1:25,000,000, *U.S. Geol. Surv. Misc. Invest. Ser., Map I-1083*.

Scott, D. H., and K. L. Tanaka (1986), Geologic map of the western equatorial region of Mars, scale 1:15,000,000, *U.S. Geol. Surv. Misc. Invest. Ser., Map I-1082-A*.

Sharpton, V. L., and J. W. Head (1988), Lunar mare ridges: Analysis of ridge-crater intersections and implications for the tectonic origin of mare ridges, *Proc. Lunar Planet. Sci. Conf. 18th*, 307–317.

Sibson, R. H. (1994), An assessment of field evidence for 'Byerlee' friction, *Pure Appl. Geophys.*, *142*, 645–662.

Simpson, R. W., and P. A. Reasenberg (1994), Earthquake-induced static stress changes on central California faults, in *The Loma Prieta, California Earthquake of October 17, 1989—Tectonic Processes and Models*, *U.S. Geol. Surv. Prof. Pap.*, *1550-F*, F55–F89.

Stein, R. S. (1999), The role of stress transfer in earthquake occurrence, *Nature*, *402*, 605–609.

Stein, R. S., G. King, and J. Lin (1992), Change in failure stress on the southern San Andreas Fault System caused by the 1992 magnitude = 7.4 Landers earthquake, *Science*, *258*, 1328–1331.

Strom, R. G. (1972), Lunar mare ridges, rings and volcanic ring complexes, in *The Moon*, edited by S. K. Runcorn and H. C. Urey, *IAU Symp. 47*, pp. 3–70, Springer, New York.

Strom, R. G., N. J. Trask, and J. E. Guest (1975), Tectonism and volcanism on Mercury, *J. Geophys. Res.*, *80*, 2478–2507.

Tanaka, K. L. (1986), The stratigraphy of Mars, *Proc. Lunar Planet. Sci. Conf.*, part 1, *J. Geophys. Res.*, *91*, suppl., E139–E158.

Tanaka, K. L., and G. J. Leonard (1995), Geology and landscape evolution of the Hellas region of Mars, *J. Geophys. Res.*, *100*, 5407–5432.

Toda, S., R. S. Stein, R. A. Reasenberg, J. H. Dieterich, and A. Yoshida (1998), Stress transferred by the 1995 Mw = 6.9 Kobe, Japan, shock: Effect on aftershocks and future earthquake probabilities, *J. Geophys. Res.*, *103*, 24,543–24,565.

Twiss, R. J., and E. M. Moores (1992), *Structural Geology*, 532 pp., W. H. Freeman, New York.

Watters, T. R. (1988), Wrinkle ridge assemblages on the terrestrial planets, *J. Geophys. Res.*, *93*, 10,236–10,254.

Watters, T. R. (1993), Compressional tectonism on Mars, *J. Geophys. Res.*, *98*, 17,049–17,060.

Watters, T. R. (2003a), Lithospheric flexure and the origin of the dichotomy boundary on Mars, *Geology*, *31*, 271–274.

Watters, T. R. (2003b), Thrust faults along the dichotomy boundary in the eastern hemisphere of Mars, *J. Geophys. Res.*, *108*(E6), 5054, doi:10.1029/2002JE001934.

Watters, T. R., and D. J. Chadwick (1989), Cross-cutting periodically spaced first-order ridges in the ridged plains of Hesperia Planum: Another case for a buckling model, *LPI Tech. Rep.*, abstract 89-06, pp. 68–69, Lunar and Planet. Inst., Houston, Tex.

Watters, T. R., and T. A. Maxwell (1986), Orientation, relative age, and extent of the Tharsis Plateau ridge system, *J. Geophys. Res.*, *91*, 8113–8125.

Watters, T. R., and M. S. Robinson (1997), Radar and photoclinometric studies of wrinkle ridges on Mars, *J. Geophys. Res.*, *102*, 10,889–10,903.

Wilkins, S. J., and R. A. Schultz (2003), Cross faults in extensional settings: Stress triggering, displacement localization, and implications for the origin of blunt troughs at Valles Marineris, Mars, *J. Geophys. Res.*, *108*(E6), 5056, doi:10.1029/2002JE001968.

Wilkins, S. J., R. A. Schultz, R. C. Anderson, J. M. Dohm, and N. H. Dawers (2002), Deformation rates from faulting at the Tempe Terra extensional province, Mars, *Geophys. Res. Lett.*, *29*(18), 1884, doi:10.1029/2002GL015391.

Wise, D. U., M. P. Golombek, and G. E. McGill (1979), Tharsis province of Mars: Geologic sequence, geometry, and a deformational mechanism, *Icarus*, *38*, 456–472.

Ziv, A., and A. M. Rubin (2000), Static stress transfer and earthquake triggering: No lower threshold in sight?, *J. Geophys. Res.*, *105*, 13,631–13,642.

C. L. Goudy and R. A. Schultz, Department of Geological Sciences and Engineering, University of Nevada, Mail Stop 172, Reno, NV 89557, USA. (schultz@mines.unr.edu)

T. K. P. Gregg, Department of Geological Sciences, University at Buffalo, Buffalo, NY 14260, USA.